

Halo-model analysis of the clustering of photometric luminous red galaxies at $0.10 \leq z \leq 1.05$ from the Subaru Hyper Suprime-Cam Survey

SHOGO ISHIKAWA,^{1,2} TEPPEI OKUMURA,^{3,4} MASAMUNE OGURI,^{4,5,6} AND SHENG-CHIEH LIN^{3,7}

¹*Center for Computational Astrophysics, National Astronomical Observatory of Japan, Mitaka, Tokyo 181-8588, Japan*

²*National Astronomical Observatory of Japan, Mitaka, Tokyo 181-8588, Japan*

³*Institute of Astronomy and Astrophysics, Academia Sinica, No. 1, Section 4, Roosevelt Road, Taipei 10617, Taiwan*

⁴*Kavli Institute for the Physics and Mathematics of the Universe (WPI), UTIAS, The University of Tokyo, Kashiwa, Chiba 277-8583, Japan*

⁵*Research Center for the Early Universe, The University of Tokyo, 7-3-1 Hongo, Bunkyo-ku, Tokyo, 113-0033, Japan*

⁶*Department of Physics, The University of Tokyo, 7-3-1 Hongo, Bunkyo-ku, Tokyo 113-0033, Japan*

⁷*Department of Physics and Astronomy, University of Kentucky, 505 Rose Street, Lexington, KY 40506, USA.*

ABSTRACT

We present the clustering analysis of photometric luminous red galaxies (LRGs) at a broad redshift range, $0.1 \leq z \leq 1.05$, selected in the Hyper Suprime-Cam Subaru Strategic Program Wide layer. The CAMIRA algorithm yields 615,317 LRGs over $\sim 124 \text{ deg}^2$ with information of stellar masses and photometric redshifts, enabling to trace the redshift and stellar-mass dependence of the baryonic and dark halo characteristics of LRGs. The halo occupation distribution analysis reveals a tight correlation between the dark halo mass of central LRGs, M_{\min} , and the number density of LRGs independently of redshifts, indicating that the formation of LRGs is associated with the global environment. The halo mass M_{\min} of the LRGs depends only weakly on the stellar mass M_{\star} at $M_{\star} \lesssim 10^{10.75} h^{-2} M_{\odot}$ and $0.3 < z < 1.05$, in contrast to the $M_{\min} - M_{\star}$ relation for all galaxies including both red and blue galaxies. This is indicative of the dark halo mass is being the key parameter for the formation of LRGs rather than the stellar mass. Our result suggests that the halo mass of $\sim 10^{12.5 \pm 0.2} h^{-1} M_{\odot}$ is the critical mass for an efficient halo quenching due to the halo environment. A comparison between our observed halo masses and the hydrodynamical simulation indicates that the low-mass LRGs at $z \sim 1$ increase their stellar masses one order magnitude across $z = 1 - 0$ through mergers and satellite accretions, and large fraction of massive LRGs at $z < 0.9$ evolve from massive green valley galaxies with short transition time scale.

Keywords: cosmology: observations — dark matter — large-scale structure of universe — galaxies: evolution — formation

1. INTRODUCTION

The formation of the large-scale structure of the Universe, which can be traced by galaxies, is largely governed by cosmology in the early Universe. Small matter density fluctuations in the early Universe evolve into biased objects, known as dark haloes, via gravitational instability. Galaxies that are an important tracer of the large-scale structure form in dark haloes by trapping baryons by their gravitational wells. Dark haloes formed in the early epoch induce cooling and condense processes

on the accreted baryonic gasses at the early stage of the Universe; therefore, highly biased galaxies tend to reside in old, massive dark haloes (e.g., [White & Rees 1978](#); [Blumenthal et al. 1984](#)).

Luminous red galaxies (LRGs) are thought to be a passively evolving, long-lived galaxy population hosted by the old dark haloes ([Eisenstein et al. 2001](#)). Hence, LRGs are a suitable tracer for studying the large-scale structure of the Universe. Since LRGs exhibit strong clustering signals due to their high brightness and early formation, many redshift surveys have collected a large number of LRGs over a broad redshift range, especially after the notable success by the Sloan Digital Sky Survey (SDSS). Then clustering of LRGs have been measured as a function of various baryonic properties of the LRGs

(e.g., Zheng et al. 2009; Reid et al. 2010; Zehavi et al. 2011; Guo et al. 2013).

Since all galaxies are considered to form within haloes in the current paradigm of cosmic structure formation, investigating galaxy clustering provides clues to understand the relationship between galaxies and host dark haloes and reveal properties of invisible underlying dark matter distribution. Furthermore, measuring and interpreting the galaxy clustering signals play an important role to unveil the unknown processes of galaxy formation and evolution (e.g., Wechsler & Tinker 2018).

Two-point auto-correlation functions (2PCFs) are commonly used to quantify clustering of galaxies (Totsuji & Kihara 1969; Peebles 1980). The 2PCF provides various information at different physical scales ranging from the large-scale structure of the Universe to the galaxy formation within dark haloes. At large physical scales, the 2PCF is approximately attributed to the matter-matter correlation function in linear regime enhanced by the halo bias (e.g., Seljak 2000; Ma & Fry 2000). On the other hand, the 2PCF at small scales contains a wealth of information on the non-linear physical processes of galaxy formation and evolution, and the central-satellite interactions within dark haloes (e.g., Kravtsov et al. 2004; Tinker et al. 2005).

Observed 2PCFs of galaxies can be interpreted using analytical halo models that are developed based on the galaxy formation model and the Λ -dominated Cold Dark Matter (Λ CDM) cosmological model (Cooray & Sheth 2002, for a review). One of the most successful halo models for analyzing the observed clustering signals is the halo occupation distribution (HOD) model (e.g., Berlind & Weinberg 2002; Berlind et al. 2003; van den Bosch et al. 2003). The HOD model characterizes the galaxy bias in terms of galaxy occupation within dark haloes, and predicts 2PCFs via the conditional probability of the number of galaxies N as a function of dark halo mass M_h , $P(N|M_h)$. LRGs selected by spectroscopic galaxy redshift surveys are succeeded in revealing the biasing relation over the underlying dark matter as well as the redshift evolution of the LRG itself (e.g., Zheng et al. 2009; White et al. 2011; Guo et al. 2013; Parejko et al. 2013; Zhai et al. 2017). However, the galaxy redshift surveys focus only on luminous galaxies in general and the redshift and stellar-mass ranges covered by the spectroscopic surveys are quite limited.

In this paper, we report the clustering properties of photometric LRGs selected by the Subaru Telescope Hyper Suprime-Cam Subaru Strategic Program (HSC SSP; Aihara et al. 2018). HSC SSP is an extensive photometric survey with deep and wide optical imaging survey

fields utilizing the capability of the wide-field imaging camera Hyper Suprime-Cam, which is mounted on the Subaru Telescope (HSC; Miyazaki et al. 2018). Deep and wide-field photometric data of the HSC SSP and the sophisticated LRG-selection algorithm (CAMIRA; Oguri 2014) enable us to construct an LRG sample for a wide range of redshift and stellar mass, where redshifts are estimated using the photometric redshift (photo- z) technique. The main purpose of this paper is to reveal the properties of LRGs as a function of the stellar mass and redshift by comparing with the results of photo- z -selected all galaxy samples containing both red and blue galaxies obtained in the HSC SSP (Ishikawa et al. 2020) through the clustering and the subsequent HOD analyses.

This paper is organized as follows. In Section 2, we present the details of our photometric data and LRG selection method using the CAMIRA algorithm (Oguri 2014; Oguri et al. 2018a), and clustering and HOD analyses of the LRG samples are shown in Section 3. Results obtained by the HOD analyses of the clustering of LRGs and comparison with the HSC all photo- z galaxy samples are given in Section 4, discussion based on the HOD analysis is presented in Section 5, and we give a conclusion in Section 6.

We employ the Planck 2015 cosmological parameters (Planck Collaboration et al. 2016); i.e., the matter, baryon, and dark energy density parameters are $\Omega_m = 0.309$, $\Omega_b = 0.049$, and $\Omega_\Lambda = 0.691$, respectively, the dimensionless Hubble parameter is $h = 0.677$, the amplitude of the linear power spectrum averaged over $8h^{-1}$ Mpc scale is $\sigma_8 = 0.816$, and the scalar spectrum index of the primordial power spectral is $n_s = 0.967$. Throughout this paper, dark halo masses and stellar masses are denoted as M_h and M_\star with their units of $h^{-1} M_\odot$ and $h^{-2} M_\odot$, respectively. All of logarithm in this paper are common logarithm with base 10.

2. DATA AND SAMPLE SELECTION

An LRG catalogue used in this study is obtained from the photometric data of the HSC SSP S16A Wide layer, which covers over ~ 174 deg 2 in total (Aihara et al. 2018). LRGs are selected by Oguri et al. (2018a,b) using the CAMIRA algorithm (Oguri 2014). The CAMIRA fits magnitudes and colors of galaxies with a stellar population synthesis (SPS) model of Bruzual & Charlot (2003) with a fixed formation redshift of $z_f = 3$ and a prior on the metallicity that depends on the stellar mass. The SPS model is designed to reproduce red-sequence in clusters of galaxies, and is also carefully calibrated such that it reproduce colors of spectroscopic LRGs accurately. Oguri et al. (2018b) apply this method to con-

struct a photometric LRG catalog in HSC SSP S16A, which consists of galaxies that are fitted well by the SPS model for LRGs. Additionally, in this paper we impose the `bright-star mask` flag to avoid noise signals originated mainly from saturated and crosstalk pixels around luminous stars on clustering signals. Furthermore, we set manual masks by visual inspection on noisy regions and edge of the survey fields to obtain a reliable LRG catalogue for clustering measurements. The final area of our survey field is $\sim 124.31 \text{ deg}^2$ and it contains 615,317 LRGs at $0.1 \leq z \leq 1.05$.

In the CAMIRA LRG catalogue, the stellar mass and the photometric redshift of each LRG, which are derived by the CAMIRA algorithm (Oguri 2014), are available. The accuracy of the photometric redshifts of CAMIRA LRGs is tested in Oguri et al. (2018b) by comparing them with the spectroscopic redshifts that have already observed by other extensive surveys. At $0.1 < z_{\text{phot}} < 1.05$, the outlier rate of the whole LRG samples is found to be $\sim 7\%$. The scatter of photometric redshifts, which is defined as a scatter of $(z_{\text{phot}} - z_{\text{spec}})/(1 + z_{\text{spec}})$ after 3σ clipping is found to be $\sim 2\%$, which is comparable to the result of LRGs selected by the redMaGiC algorithm (Rozo et al. 2016). Interested readers are referred to Oguri (2014) and Oguri et al. (2018a,b) for more details of the original CAMIRA LRG catalogue and its photometric-redshift performance.

The LRG sample is divided into subsamples according to their stellar masses and photometric redshifts. The stellar mass versus redshift diagram is shown in Figure 1. We adopt the similar binning along the redshift of Ishikawa et al. (2020) for comparisons of physical characteristics of our LRGs with photo- z -selected all galaxy samples containing both red and blue galaxies (hereafter photo- z galaxies) obtained in the same dataset of HSC SSP S16A Wide layer. The redshift distribution of LRGs is shown in the top panel of Figure 2 and details of each subsample are presented in Table 1.

In addition, we also generate a random-point catalogue that covers the entire field of the LRG catalogue. The surface density of the random catalogue is set as $\sim 35 \text{ arcmin}^{-2}$, which is ~ 100 times larger than that of the LRG catalogue, in order to reduce the Poisson noise on clustering signals. The random points are excluded around bright stars and near edges of the fields as is in the case with the LRG catalogue.

3. CLUSTERING AND HOD ANALYSIS

3.1. Angular Auto-correlation Function

We measure angular auto-correlation functions (ACFs) of the LRG samples. The ACFs are calculated using an

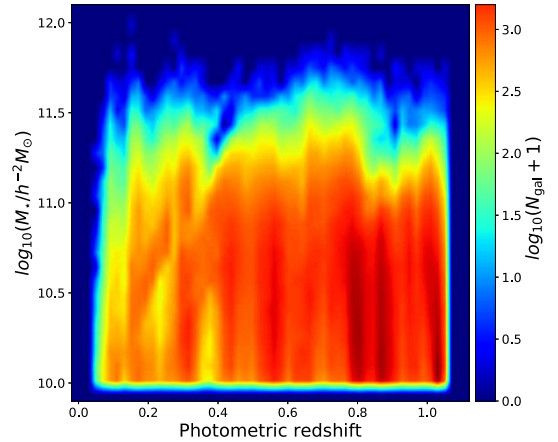


Figure 1. The stellar mass versus redshift diagram of the HSC SSP S16A photometric LRG sample used in this paper. Color indicates the differential abundance of LRGs in logarithmic scale at each cell.

estimator proposed by Landy & Szalay (1993) as:

$$\omega(\theta) = \frac{\text{DD} - 2\text{DR} + \text{RR}}{\text{RR}}, \quad (1)$$

where DD, DR, and RR denote the numbers of normalized pairs of galaxy-galaxy, galaxy-random, and random-random with separation angle of $\theta \pm \delta\theta$, respectively. In this study, a range of the ACF angular scale is $-3.4 \leq \log_{10}(\theta) \leq 0.0$ with the angular separation of $\log_{10}(\delta\theta) = 0.1$ in a degree scale.

An observed galaxy correlation function is underestimated at large-angular scales due to the finite survey field, known as the integral constraint (IC) (e.g., Groth, & Peebles 1977). We first calculate this effect by Monte Carlo integration as:

$$\text{IC} = \frac{\sum_i \theta_i^{1-\gamma} \text{RR}(\theta_i)}{\sum_i \text{RR}(\theta_i)}, \quad (2)$$

assuming that the ACF can be modeled by a power-law form (Roche, & Eales 1999). The unbiased ACFs, ω_{true} , can be evaluated by correcting the observed ACFs, ω_{obs} , as:

$$\omega_{\text{true}}(\theta) = \omega_{\text{obs}}(\theta) \frac{\theta^{1-\gamma}}{\theta^{1-\gamma} - \text{IC}}, \quad (3)$$

where γ is the power-law index, $\omega(\theta) \propto \theta^{-\gamma}$.

We use the jackknife resampling method to evaluate errors of the ACFs (e.g., Norberg et al. 2009). We divide our survey field into 123 subfields, each of which covers $\sim 1 \text{ deg}^2$, and calculate the ACFs 123 times, removing each subfield. The covariance matrix can be computed

Table 1. Details of Cumulative Stellar-mass Limited Subsamples

Stellar-mass limit ^a	z ₁			z ₂			z ₃			z ₄		
	0.10 ≤ z < 0.30			0.30 ≤ z < 0.55			0.55 ≤ z < 0.80			0.80 ≤ z ≤ 1.05		
	N ^b	M _{*,med} ^c	n _g ^d	N	M _{*,med}	n _g	N	M _{*,med}	n _g	N	M _{*,med}	n _g
10.00	56,249	10.53	9.12	132,223	10.59	5.07	196,623	10.57	3.76	230,222	10.48	3.07
10.25	41,586	10.67	6.50	107,664	10.68	4.10	158,538	10.67	3.03	170,292	10.61	2.24
10.50	29,693	10.79	4.55	78,205	10.80	3.17	112,600	10.80	2.16	110,352	10.74	1.45
10.75	16,863	10.96	2.48	45,071	10.95	1.67	65,009	10.96	1.22	52,779	10.90	0.66
11.00	6,967	11.13	1.00	17,740	11.12	0.64	27,035	11.14	0.51	13,726	11.09	0.17

^aThreshold stellar mass of each subsample in units of $h^{-2}M_{\odot}$ in a logarithmic scale.

^bThe number of LRGs of each subsample.

^cMedian stellar mass of each subsample in units of $h^{-2}M_{\odot}$ in a logarithmic scale.

^dLRG number density in units of $10^{-3}h^{-3}\text{Mpc}^3$

as:

$$C_{ij} = \frac{N-1}{N} \sum_{k=1}^N (\omega_k(\theta_i) - \bar{\omega}(\theta_i)) (\omega_k(\theta_j) - \bar{\omega}(\theta_j)), \quad (4)$$

where $N = 123$, C_{ij} is an (i, j) element of the covariance matrix, $\omega_k(\theta_i)$ is the ACF of the i th angular bin of the k th jackknife realization, and $\bar{\omega}(\theta_i)$ is the ACF with the i th angular bin averaged over the N realizations, $\bar{\omega}(\theta_i) = N^{-1} \sum_{k=1}^N \omega_k(\theta_i)$.

3.2. HOD Analysis

3.2.1. Methodology

We use an HOD formalism for interpreting the observed ACFs and link the LRGs to their host dark haloes (e.g., Seljak 2000; Berlind & Weinberg 2002). The HOD model parameterizes the occupation of galaxies as a function of dark halo mass and predicts galaxy correlation functions according to the assumed galaxy distribution within dark haloes. In this study, we adopt the standard galaxy occupation function proposed by Zheng et al. (2005) for the distribution of our LRG samples within dark haloes. The total number of LRGs within a dark halo with mass M_h , $N_{\text{tot}}(M_h)$, can be decomposed into the central and satellite components, N_c and N_s , respectively, and described as:

$$N_{\text{tot}}(M_h) = N_c(M_h) [1 + N_s(M_h)]. \quad (5)$$

In the HOD model of Zheng et al. (2005), the occupations of central and satellite galaxies are written as:

$$N_c(M_h) = \frac{1}{2} \left[1 + \text{erf} \left(\frac{\log_{10} M_h - \log_{10} M_{\min}}{\sigma_{\log M}} \right) \right], \quad (6)$$

$$N_s(M_h) = \left(\frac{M_h - M_0}{M_1} \right)^\alpha. \quad (7)$$

There are five free HOD parameters in the above occupation functions; M_{\min} is the characteristic mass to host a central galaxy, M_1 is a mass for a halo with a central galaxy to host one satellite, M_0 is the mass scale to truncate satellites, $\sigma_{\log M}$ is the characteristic transition width, and α is the slope of the power law for the satellite HOD. Once a set of these parameters is given, one can uniquely compute the three-dimensional power spectrum which is then converted to the angular correlation function, $\omega_{\text{HOD}}(\theta)$. Previous studies successfully reproduced galaxy clustering of LRGs (e.g., Zheng et al. 2009; Zhai et al. 2017) and massive red galaxies (e.g., Brown et al. 2008; Matsuoka et al. 2011) at $z < 1$ using the above occupation functions.

The HOD parameters are constrained by comparing the observed ACF with the predicted one from the HOD model using the χ^2 statistic. The χ^2 is computed as:

$$\chi^2 = \sum_{i,j} [\omega_{\text{true}}(\theta_i) - \omega_{\text{HOD}}(\theta_i)] (C_{ij}^{-1}) [\omega_{\text{true}}(\theta_j) - \omega_{\text{HOD}}(\theta_j)] + \frac{(n_g^{\text{obs}} - n_g^{\text{HOD}})^2}{\sigma_{n_g}^2}, \quad (8)$$

where $\omega_{\text{HOD}}(\theta_i)$ is the ACFs of i th angular bin from the HOD model, n_g^{obs} is the observed number density of galaxies (see Table 1) and σ_{n_g} is its uncertainty. The quantity n_g^{HOD} is the number density predicted by a given HOD model,

$$n_g^{\text{HOD}} = \int dM_h \frac{dn}{dM_h} N(M_h), \quad (9)$$

where dn/dM_h is a halo mass function. In calculating the inverse covariance matrix, C_{ij}^{-1} , from equation (4), we apply a correction factor presented by Hartlap et al. (2007) to avoid underestimating the inverse covariance due to the finite realization effect.

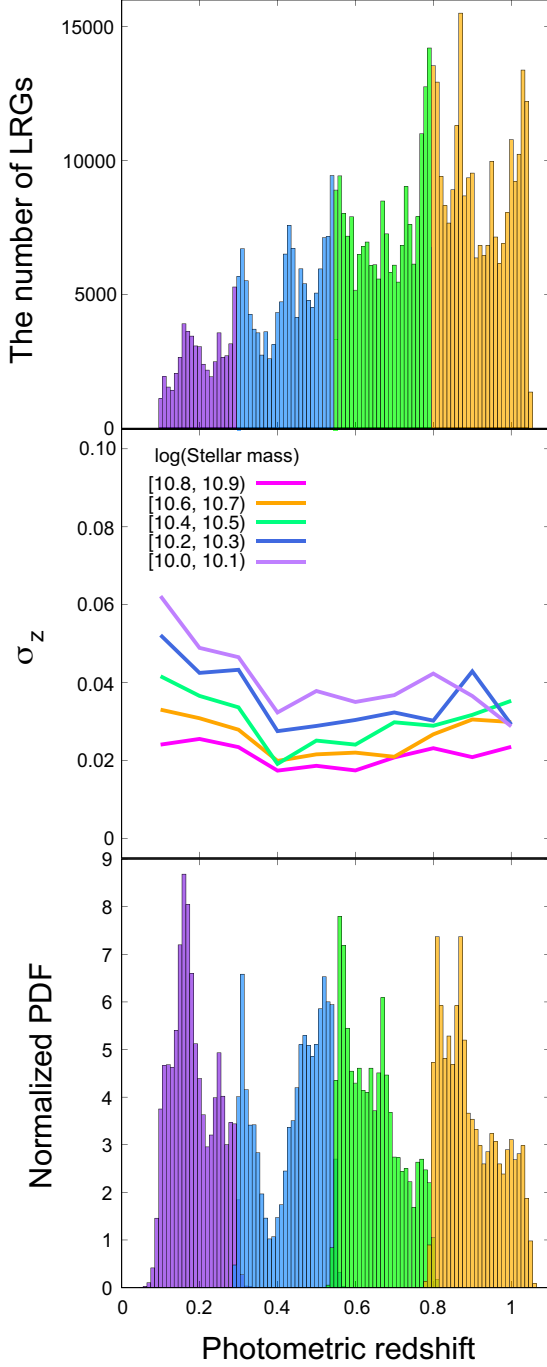


Figure 2. Top: Redshift distribution of the LRG sample. LRGs are divided into four redshift bins: $0.10 \leq z < 0.30$ (purple), $0.30 \leq z < 0.55$ (blue), $0.55 \leq z < 0.80$ (green), and $0.80 \leq z \leq 1.05$ (orange). Middle: Scatter of photometric redshifts as a function of the photometric redshift. These scatters are evaluated after the exclusion of outlier LRGs. Different colors indicate the difference of stellar-mass slices. Bottom: Redshift distribution of total LRGs at each redshift bin that takes account of the photo- z errors. Colors indicate the same redshift divisions used in the top panel.

The uncertainty of the observed number density, σ_{n_g} , takes account of the effect of the photometric redshift errors. While it has been confirmed that the CAMIRA LRG samples are less affected by the photometric-redshift uncertainties compared to all photo- z galaxies, we conservatively introduce 10% uncertainties on the galaxy abundance that takes account of the photometric-redshift errors and some of unknown systematic biases as is the case with Zhou et al. (2021).

To predict ACFs from the HOD framework, one needs to calculate several quantities analytically. We employ a halo mass function proposed by Sheth, & Tormen (1999), an NFW profile (Navarro et al. 1997) as a density profile of dark haloes, the mass and redshift dependence of a concentration parameter presented by Takada, & Jain (2003), and a large-scale halo bias of Tinker et al. (2010) with a halo exclusion effect (Zheng 2004; Tinker et al. 2005). We use the non-linear power spectrum of Smith et al. (2003) with a matter transfer function of Eisenstein, & Hu (1998).

3.2.2. Photo- z error estimation

Although the redshift distributions of LRGs using the best-fitting photometric redshifts are already evaluated in the top panel of Figure 2, they could be biased from the true redshift distributions of LRGs due to the underestimation of the tails of the redshift bins and uncertainties of photometries. Therefore, it is essential that the redshift distribution that is used in the HOD-model analysis should consider errors of photometric redshifts to reconstruct observed ACFs. To take account of the photo- z errors that induce outer skirts of the distribution at each redshift bin in the interpretation of observed clustering, we recalculate redshift distributions of LRGs by considering those uncertainties.

The redshift distribution of the LRGs including photo- z errors is evaluated as follows. First, we focus on the LRGs whose spectroscopic redshifts have been already measured by extensive other surveys and calculate the scatter of photometric redshifts σ_z of the residual of both redshifts, i.e., $(z_{\text{phot}} - z_{\text{spec}})/(1 + z_{\text{spec}})$, where z_{phot} and z_{spec} respectively represent photometric and spectroscopic redshifts of each LRG. The photo- z scatter is evaluated by calculating the root mean square of the residual after excluding the outlier LRGs that satisfy $|z_{\text{phot}} - z_{\text{spec}}|/(1 + z_{\text{spec}}) > 0.15$. It should be noted that the LRGs with spec- z information account for only $\sim 5.3\%$ of the total LRG sample, and the fraction of outlier LRGs to those whose spec- z 's are available is $\sim 2.2\%$, respectively. The scatter of photo- z is estimated by binning along the both stellar masses and redshifts simultaneously, with bin sizes of

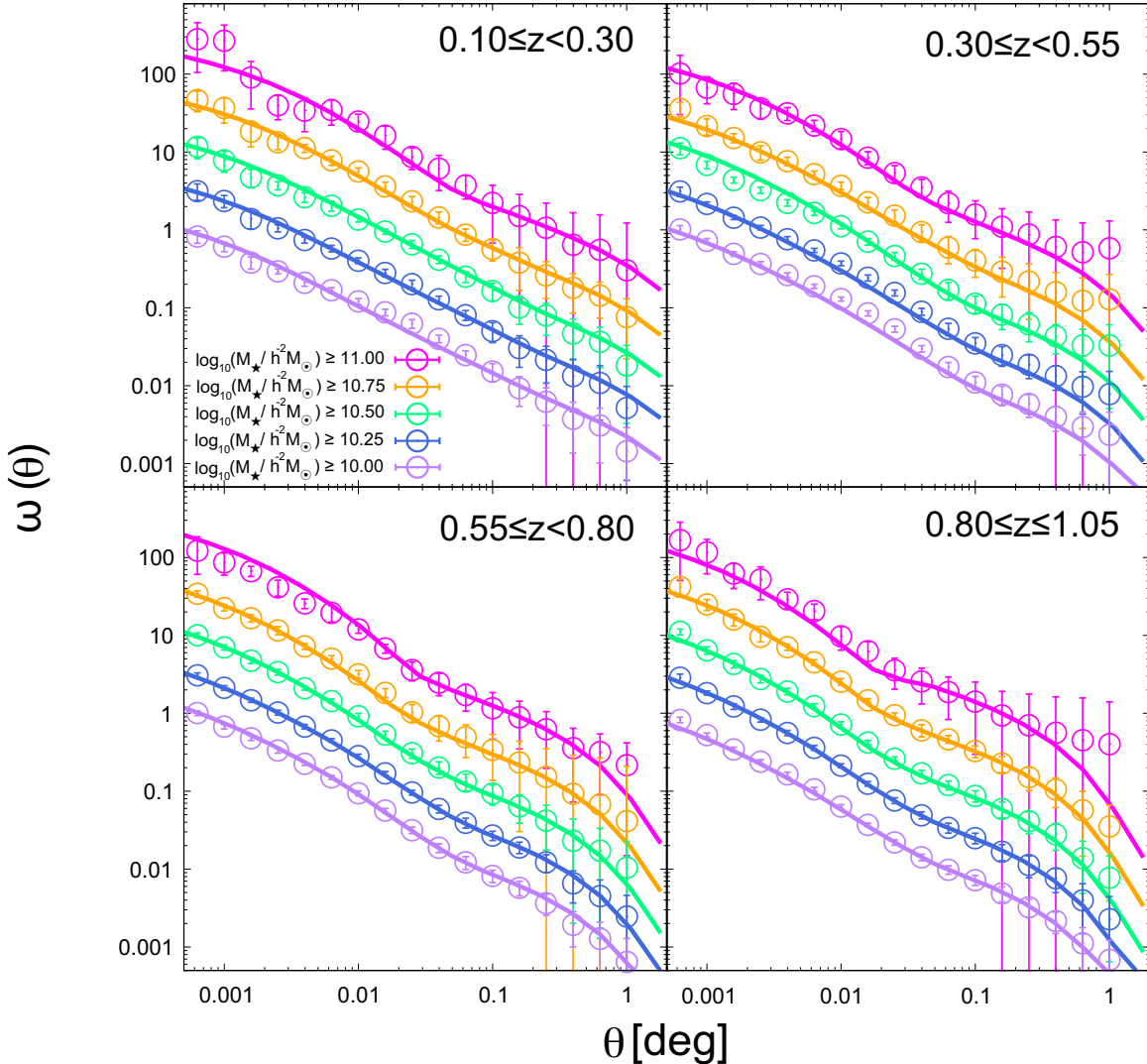


Figure 3. Observed ACFs of LRGs (circles) and their best-fitting ACFs derived by the HOD model (solid lines) at $0.10 \leq z < 0.30$ (top left panel), $0.30 \leq z < 0.55$ (top right panel), $0.55 \leq z < 0.80$ (bottom left panel), and $0.80 \leq z \leq 1.05$ (bottom right panel) redshift bins, respectively. In the HOD fitting procedure, correlations between angular bins are taken into consideration by covariance matrices calculated by the jackknife resampling method. For clarity, amplitudes of ACFs are normalized arbitrarily.

$\delta \log_{10}(M_*/M_\odot) = 0.1$ and $\delta z = 0.1$, respectively. The middle panel of Figure 2 represents the scatter of photometric redshifts with various stellar-mass slices as a function of the photometric redshift. As expected, less massive and high- z LRGs tend to have relatively larger uncertainties in their photo- z estimation.

Using the estimated photo- z scatter, photometric redshifts of each LRG are randomly reassigned using the photo- z scatter and we repeatedly implement this procedure 100 times in order to obtain averaged redshift distributions considering photo- z errors of each LRG. The bottom panel of Figure 2 is the LRG redshift distributions of each redshift bin considering the photo- z errors obtained by the above procedure. These redshift

distributions including the photo- z errors are used in the following HOD analysis.

3.2.3. HOD-model fitting

We implement the HOD-model fitting on the LRG samples. Results are shown in Figure 3 and the best-fitting parameters are listed in Table 6. The HOD model successfully reproduces the observed ACFs of LRGs over the whole ranges of the angular scales, the stellar mass, and the redshift explored in this paper. The HOD halo mass parameters M_{\min} and M_1 are strongly constrained due to the strong clustering signals thanks to the accurate photometric redshift as well as the advantage of the large sample size achieved by the large survey volume of the HSC SSP.

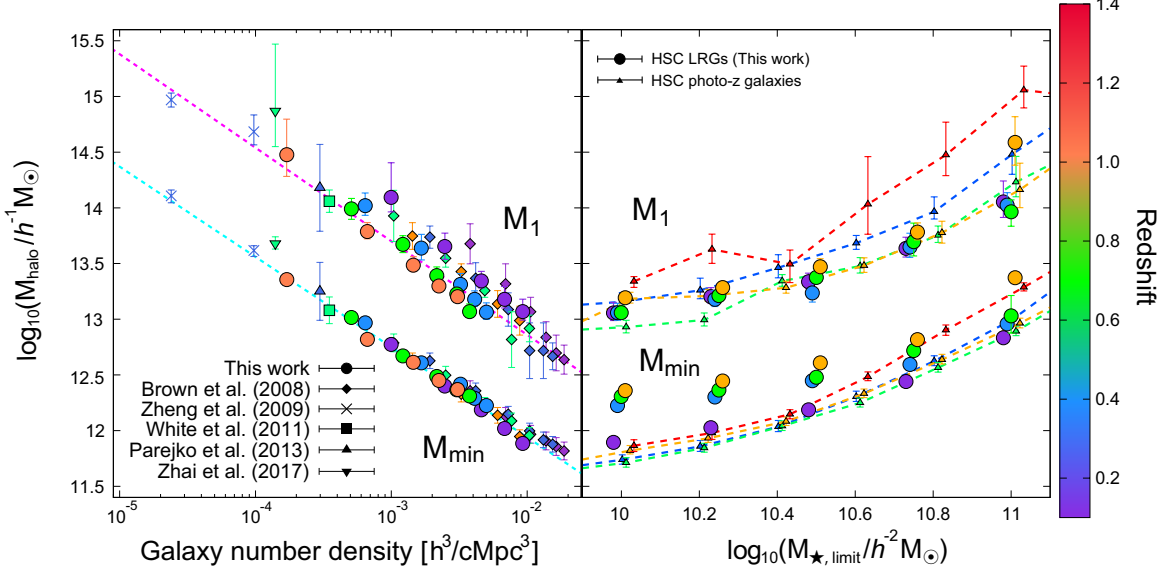


Figure 4. Left: Observed HOD halo mass parameters (M_{min} and M_1 in logarithmic scales) of LRGs as a function of the number density of galaxies. Colors show the difference of redshift range and similar color between our results and previous studies indicates the comparable redshift range (refer to the color bar on the right side of the figure). Dashed cyan and magenta lines are best-fitted power-law slopes of our M_{min} and M_1 , respectively. Right: HOD halo mass parameters (M_{min} and M_1 in logarithmic scales) of LRGs (circles) and HSC photo-z galaxies (triangles) as a function of the stellar-mass threshold. Colors show the difference of redshift ranges. Symbols are slightly shifted toward horizontal axis for clarity.

4. RESULTS

In this section, we present constraints on the physical parameters of LRGs and their host halos based on the HOD modeling. We show the results of constraints on the halo mass parameters, M_{min} and M_1 , in Figure 4, the satellite fraction of LRGs, f_s , in Figure 5, and the large-scale galaxy bias, b_g , in Figure 6. In each figure, the left panel compares our constraint to those for LRGs from previous studies with different surveys (Brown et al. 2008; Zheng et al. 2009; White et al. 2011; Parejko et al. 2013; Zhai et al. 2017) as a function of the number density. The right panel compares our constraint to that for the photo- z galaxies from the same HSC survey (Ishikawa et al. 2020) as a function of the stellar mass threshold. We will discuss these results in more detail in the following subsections.

4.1. M_{min} and M_1

Here we investigate the redshift evolution of the HOD halo mass parameters, M_{min} and M_1 . By definition, M_{min} is a halo mass for which the expected number of central galaxy occupation is 50%, whereas M_1 is a typical halo mass that is expected to possess one satellite galaxy. We do not discuss the other halo mass parameter in our HOD model, M_0 , since it has large uncertainties ($\sim \pm 2$ dex errors in typical cases).

First, we compare the constraints on M_{min} and M_1 for CAMIRA LRGs with those for LRGs from previous HOD studies to confirm the consistency among them.

Thanks to the wide survey area and sufficient deep imaging data of the HSC SSP Wide layer, we successfully determine the HOD halo mass parameters for wide stellar mass and redshift ranges as shown in the left panel of Figure 4. Our constraints, particularly on M_{min} , show excellent agreement with the previous studies. The constrained values of M_{min} and M_1 are strongly correlated with the number density of LRGs and approximated as a single power law with decreasing the number density, $M_{\text{min}} \propto n_g^{-0.8}$ and $M_1 \propto n_g^{-1.0}$, depicted by the cyan and magenta lines, respectively. This result indicates that the formation efficiency of massive satellite LRGs is much lower than that of massive central LRGs at each epoch. Interestingly, while the parameter M_{min} does not depend on redshift, M_1 is constrained to have slight redshift evolution for a given number density; i.e., LRGs at lower redshift have slightly larger M_1 at a fixed number density.

Next, we compare in the right panel of Figure 4 our constraints on the HOD mass parameters for LRGs to those for the different population, photo- z galaxies, obtained from the same HSC survey (Ishikawa et al. 2020). The stellar masses and photometric redshifts of the HSC photo- z galaxies are evaluated through a template SED-fitting technique with Bayesian priors on the galaxy physical properties (MIZUKI; Tanaka 2015). The photo- z galaxies are selected using the same dataset as the one used in this study, which are obtained in the HSC SSP Wide layer S16A, without imposing any color cuts

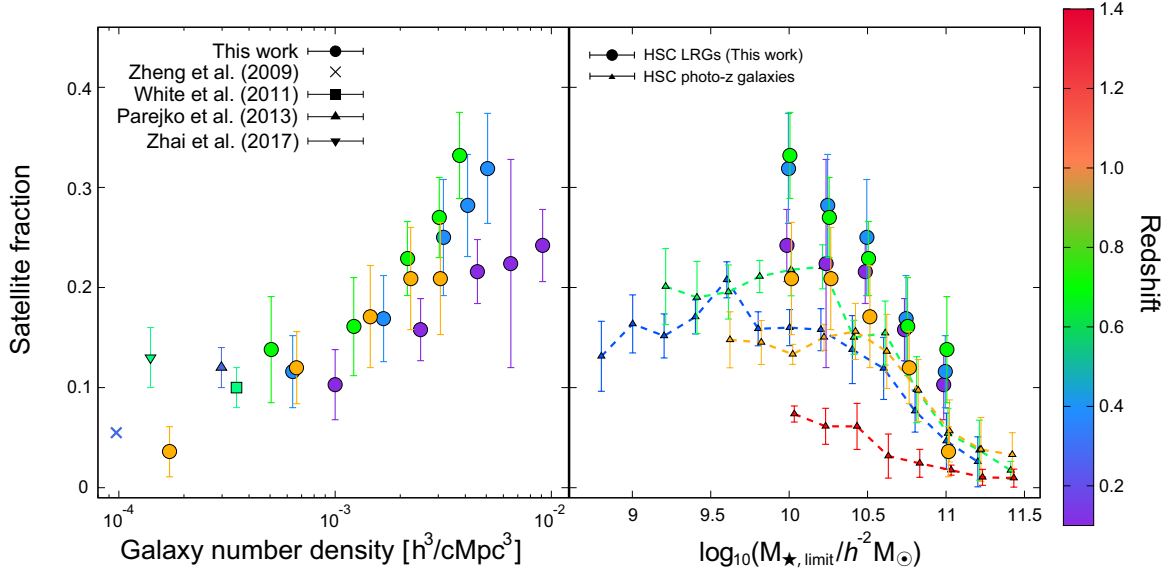


Figure 5. Similar to Figure 4, but for the satellite fraction.

as with this study. Hence, our LRG sample is a subset of the whole HSC photo- z galaxy sample. It should be noted that the assumed initial mass functions (IMFs) for the stellar-mass estimation are different between LRGs and photo- z galaxies; i.e., stellar masses of LRGs are evaluated assuming the Salpeter IMF (Salpeter 1955), whereas those of photo- z galaxies are estimated assuming the Chabrier IMF (Chabrier 2003). We multiply by a factor of 1.65 to the stellar masses of the photo- z galaxies to account for the offset of stellar masses introduced by the different IMFs.

One of the largest differences between two populations is that M_{\min} of LRGs increases less with the stellar-mass threshold except for the lowest- z results, indicating that the dark halo mass is the key parameter for the formation of central LRGs. Many studies have argued galaxy quenching models for evolving into the red-sequence galaxies: the mass quenching (e.g., Peng et al. 2010, 2012; Geha et al. 2012) and the environmental quenching (e.g., Gunn & Gott 1972; van den Bosch et al. 2008; Wetzel et al. 2013), and various physical mechanisms have been proposed to cease star formation according to their stellar masses and/or dark halo masses (i.e., mass quenching) such as a hot-halo quenching due to the virial-shock heating (e.g., Birnboim & Dekel 2003; Dekel et al. 2009) and the radio-mode AGN feedback (e.g., Kereš et al. 2009; Gabor et al. 2011). We will discuss the relation of M_{\min} to the quenching models and the formation scenario of LRGs in Section 5.

In addition, values of M_{\min} for LRGs are significantly larger than those for photo- z galaxies in the less-massive end. The HSC photo- z galaxies consist of both star-forming and passive galaxies and it is plausible that less-

massive central LRGs reside in massive dark haloes compared to less-massive photo- z galaxies whose red fractions are expected to be small.

In contrast to M_{\min} , M_1 of LRGs shows the stellar-mass dependence similar to that obtained for the photo- z galaxies. Our results show that M_1 of LRGs evolves little at a fixed stellar mass, whereas those of photo- z galaxies appear to have redshift dependence. However, M_1 contains relatively large uncertainties compared to M_{\min} and it is difficult to draw a concrete conclusion from the current observational results.

4.2. Satellite fraction

In this subsection let us focus on the fraction of LRGs that are satellites, which can be determined from the constrained HOD parameters. A satellite fraction f_s can be calculated as:

$$f_s = 1 - f_c \\ = 1 - \frac{1}{n_g^{\text{HOD}}} \int dM_h \frac{dn}{dM_h} N_c(M_h), \quad (10)$$

where f_c represents the fraction of central galaxies. In the left panel of Figure 5, we show the satellite fraction of LRGs as a function of the number density and compare them with previous studies. Although we have no data of previous studies reaching our abundant number densities ($n_g > 10^{-3} (h/\text{cMpc})^3$), satellite fractions obtained by Zheng et al. (2009) and White et al. (2011) appear to be consistent with ours by extrapolating our f_s values to lower number density results. The satellite fraction of Zhai et al. (2017) is larger than the other studies as well as our extrapolated result; however, it is reasonable considering that the discrepancy is at most

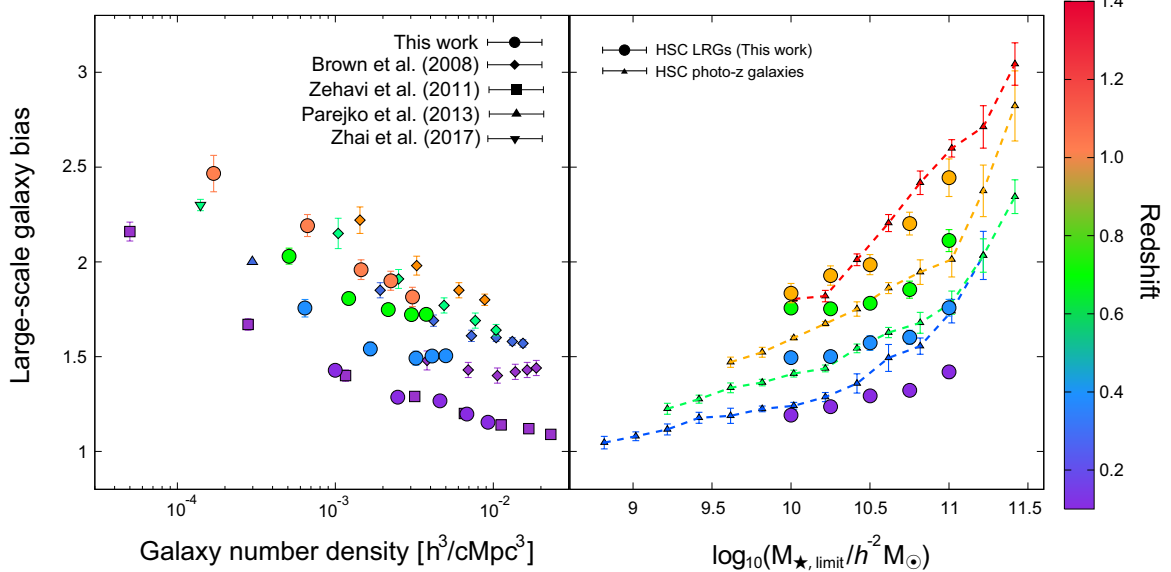


Figure 6. Similar to Figure 4, but for the large-scale galaxy bias.

$\sim 1.5\sigma$ level and the uncertainties of the satellite fractions are relatively large.

Differences of the satellite fraction between LRGs and photo- z galaxies are presented in the right panel of Figure 5. We find that, when compared for the same stellar mass limit, satellite fractions of the LRGs are higher than those of the photo- z galaxies irrespective of their stellar-mass and redshift ranges, suggesting that systems that consist of a central LRG and its satellite LRG(s) are much more common than average at least up to $z = 1.05$. Observational studies have found that physical characteristics of galaxies correlate with nearby galaxies and/or their environments, known as a galactic conformity effect (e.g., Weinmann et al. 2006; Kauffmann et al. 2010). The 1-halo conformity, which is an association of physical properties with galaxies within the same dark haloes, is well studied at $z < 1$, which indicates that passive satellite galaxies are likely to be hosted by passive central galaxies (Hartley et al. 2015; Berti et al. 2017). The higher values of LRG satellite fractions imply that the environmental quenching is effective for the wide stellar-mass range even for massive galaxies like LRGs. In addition, LRGs are known as a galaxy population that formed in high-redshift Universe and observed in their old and passively evolving phase (e.g., Eisenstein et al. 2001). Therefore, substantial satellite fraction of LRGs can be induced by merging events experienced in their long evolving history.

4.3. Galaxy bias

In this subsection we discuss the relationship of the spatial clustering between galaxies and underlying dark matter. A large-scale galaxy bias, b_g , can be evaluated

through a set of given HOD parameters as:

$$b_g = \frac{1}{n_g^{\text{HOD}}} \int dM_h b_h(M_h) \frac{dn}{dM_h} N(M_h), \quad (11)$$

where $b_h(M_h)$ is the large-scale halo bias (Tinker et al. 2010).

The galaxy biases calculated for our LRG sample using the equation (11) and those in literature are presented in the left panel of Figure 6. Our results are in good agreement with those of Zehavi et al. (2011), Parejko et al. (2013), and Zhai et al. (2017); however, galaxy biases measured by Brown et al. (2008) are systematically larger than the other results. A possible reason causing this discrepancy is the difference of procedures in the LRG selection. Studies using data obtained in the SDSS adopt a color selection described in Eisenstein et al. (2001), which is based on the SDSS $ugriz$ optical magnitudes (Fukugita et al. 1996), and the CAMIRA algorithm is also calibrated to select red-sequence galaxies using the same colors in the LRG selection of the SDSS. However, Brown et al. (2008) selected red galaxies from the bimodal galaxy distribution on the rest-frame ($U - V$) color versus V -band absolute magnitude diagram presented by Bell et al. (2004). Therefore, physical characteristics of galaxies of Brown et al. (2008) can be slightly different from other LRG studies, which might explain the difference mentioned above. In addition, difference of the cosmological parameters can enhance the discrepancy in interpretation of galaxy bias from the observed ACFs. We repeated our HOD analysis of the LRG sample at each redshift bin adopting the *WMAP3* cosmologies (Spergel et al. 2007), as adopted by Brown et al. (2008),

and found that the resulting galaxy biases increase by a few percents on average compared to our original analysis. Hence, the gap of the galaxy biases is attributed to the difference of cosmological parameters as well as the the difference of the physical characteristics of each population.

We compare the galaxy biases of the LRGs with those of the photo- z galaxies in the right panel of Figure 6. Our results show that the less massive LRGs satisfying $M_{\star} \lesssim 10^{10.5} h^{-2} M_{\odot}$ weakly depend on stellar masses and the galaxy biases drastically increase at the massive ends. The stellar-mass dependence of the photo- z galaxies is similar to the results of the LRGs; however, the galaxy biases of the photo- z galaxies at $10^{10.0} \lesssim M_{\star,\text{limit}}/h^{-2} M_{\odot} \lesssim 10^{10.5}$ increase much more with the stellar mass, which is consistent with the behavior of M_{\min} . The drastic increase of the galaxy biases of the LRGs indicates that only the most massive LRGs are highly biased objects in low- z , whereas even the intermediate-mass LRGs ($M_{\star} \sim 10^{10.5} h^{-2} M_{\odot}$) are rare at $z \sim 1$.

5. DISCUSSION

5.1. Correlation between LRG formation and dark halo mass

As shown in Figure 5, the satellite fraction of the LRGs is much higher compared to the all galaxy sample at fixed stellar masses, indicating that the LRGs tend to reside in more dense regions compared to galaxies with the same stellar masses. Observational studies have found that the galaxy quenching is much efficient in dense regions (e.g., Peng et al. 2010, 2012), and this environmental quenching effect can be triggered by the galaxy harassment (Moore et al. 1996) and the ram-pressure stripping (Gunn & Gott 1972). Therefore, the environmental quenching that originates from the local high-density environments of LRGs can play an important role of the formation of LRGs.

Interestingly, we also find that the dark halo masses of central LRGs (i.e., M_{\min}) have strong correlation with the number density of the LRGs at $0.1 < z < 1.05$ (Figure 4), although the environmental quenching is the effect caused by the interactions with surrounding galaxies. This may imply that the global environment as well as the local environment can have an impact on the galaxy quenching. The physical mechanisms of the global environmental effect and discussion about that are beyond the scope of this study; however, our results suggest that the LRG formation appears to largely depend on the local/global environments and host halo masses.

In addition, Figure 4 shows that the halo masses of central LRGs are almost constant at $M_{\star} \lesssim 10^{10.75} h^{-2} M_{\odot}$ at $z > 0.3$ and this fact supports the idea that the halo mass is the key parameter for the galaxy quenching mechanism and the formation of LRGs. The halo quenching is also the galaxy quenching model by external effects that is caused by the disturbance of star-forming activities by effects such as the virial shock heating (e.g., Birnboim & Dekel 2003; Dekel & Birnboim 2006). Our results suggests that $M_{\text{h}} \sim 10^{12.5 \pm 0.2} h^{-1} M_{\odot}$ is the threshold dark halo mass such that galaxies hosted by those dark haloes are efficiently transformed into the LRGs irrespective of those baryon properties, which is consistent with the conclusion of Woo et al. (2013).

In short, the formation of LRGs is largely connected to the environment of host dark haloes of LRGs, but the internal effect, such as the AGN feedback, can also contribute to the suppression of star formation to some extent. Our results suggest that $M_{\text{h}} \sim 10^{12.5 \pm 0.2} h^{-1} M_{\odot}$ is the critical halo mass for formation of LRGs; however, this is true at least for LRGs with stellar masses of $M_{\star} \lesssim 10^{10.75} h^{-2} M_{\odot}$ at $z > 0.3$. It is necessary to investigate the reason of the difference at $z < 0.3$ and the formation model of the most massive LRGs in future.

5.2. Halo mass accretion history and LRG evolution

Evolution of the dark halo mass is a good proxy for evolution of galaxies. In this subsection, we trace the evolution of median dark halo masses of central LRGs, i.e., M_{\min} , from $z \sim 1$ to $z = 0$ for connecting our LRGs at the highest- z bin with those at lower- z bins using the IllustrisTNG simulation (Springel et al. 2018).

We use the TNG100 simulation, which well reproduces observational stellar-mass functions even at $z \sim 1$ (Pillepich et al. 2018), and the definition of the stellar mass is the total mass of stellar particles within twice the stellar half mass radius obtained by the SUBFIND algorithm (Springel et al. 2001), while that of the halo mass is the total mass of dark matter particles that consists of dark haloes identified by the friend-of-friend algorithm. Red-sequence galaxies from the TNG100 simulation are selected according to their stellar masses, star-formation rates, and redshifts shown by the PRIMUS survey (Moustakas et al. 2013) at $z = 0.92$, which corresponds to the effective redshift of our z_4 redshift bin, and three stellar-mass limited samples are prepared that satisfy $\log_{10}(M_{\star,\text{limit}}/h^{-2} M_{\odot}) \geq 10.0, 10.5$, and 11.0 . Then we trace the halo mass of each TNG red-sequence galaxies to $z = 0$ and evaluate the evolutionary history of median halo mass of each stellar-mass limited samples at each redshift.

Solid lines and shade regions of Figure 7 show the evolution of the median halo masses and those root mean squares obtained in the IllustrisTNG simulation. It should be noted that the LRGs from the simulation are selected only at $z = 0.92$ satisfying the stellar-mass limits of $\log_{10}(M_{\star, \text{limit}}/h^{-2}M_{\odot}) \geq 10.0$ (blue), 10.5 (green), and 11.0 (red), and evolutionary tracks of halo masses indicate the mass assembly history of those LRGs from $z = 0.92$ to today.

First, let us check the consistency of the median halo masses at $z = 0.92$. We find that the median halo masses of our observed LRGs (circles) show excellent agreement with those from the simulation (right edges of the solid lines). This indicates that the mass measurement by our HOD analysis provides plausible results at least in z_4 bin. Then we investigate the relationship between HSC LRGs at $z = 0.92$ and $z < 0.92$ by comparing the observed halo masses with evolutionary history of median halo masses over $0 \leq z \leq 0.92$. From the standpoint of the halo mass evolution, the low-mass LRGs at z_4 can evolve into the intermediate-mass LRGs at z_2 and z_3 bins and finally to be the high-mass LRGs at z_1 . LRGs are thought to be passively evolving galaxies but this result indicates that low-mass LRGs at $z = 0.92$ increase their stellar masses by an order of magnitude across $z = 0.9 - 0.0$. Redshift dependence of the satellite fraction (the right panel of Figure 5) shows that the satellite fraction increases from $z \sim 1$ to $z \sim 0.3$ and then decreases to $z \sim 0.1$ at fixed stellar-mass thresholds. One explanation for the stellar mass evolution of low-mass LRGs is that they grow their stellar masses through mergers with increasing their satellite LRGs at $0.3 < z < 0.9$, and then satellite LRGs accrete onto the central LRGs at $z < 0.3$.

Next, let us see the evolution of high-mass LRGs at $z = 0.92$. The halo mass of high-mass central LRGs at z_4 is expected to reach $\sim 10^{14}h^{-1}M_{\odot}$ at $z = 0$, which corresponds to the halo masses of galaxy clusters; therefore, progenitors of BCGs of the local clusters can be the massive LRGs at $z \sim 1$. However, Banerji et al. (2010) showed that massive LRGs with stellar masses of $M_{\star} > 10^{11}M_{\odot}$ complete their stellar mass assembly by $z \sim 0.8$. The gap between our observed halo masses of massive LRGs at $z < 0.9$ and the halo mass evolution of massive LRGs at $z = 0.92$ (red line) appears to be problematic since halo masses of massive LRGs at $z < 0.9$ should be on the red line if massive LRGs truly little evolve from $z \sim 0.8$. This problem can be resolved when massive LRGs form in short time scale. A part of LRGs with $M_{\star} > 10^{11.0}h^{-2}M_{\odot}$ at $z < 0.9$ are surely descendants of massive LRGs at $z = 0.92$ and the individual halo masses of those LRGs should be near the

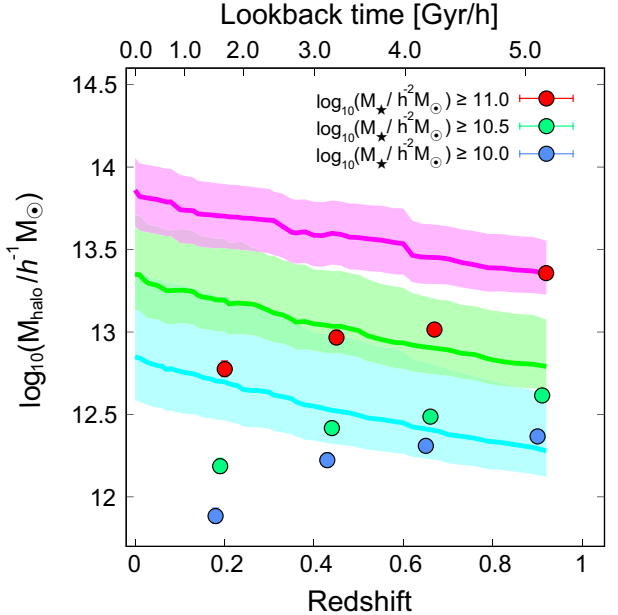


Figure 7. Evolution of median dark halo masses as a function of redshift. Circles are M_{\min} of the HSC LRGs with different stellar-mass thresholds. Lines indicate median halo mass accretion histories traced by the IllustrisTNG simulation and shade regions show the root mean squares of the halo masses in the simulation at each redshift. It is noted that the LRG-like galaxies in the IllustrisTNG are selected by being imposed the same stellar-mass threshold of circles with corresponding colors at $z = 0.92$. Our result implies that a halo which hosts LRGs with the stellar mass of $M_{\star} \geq 10^{10}h^{-2}M_{\odot}$ at $z = 0.9$ tends to host those with $M_{\star} \geq 10^{11}h^{-2}M_{\odot}$ at $z = 0$.

red line. However, there is no compromise if most of the massive LRGs at $z < 0.9$ evolve from massive green valley galaxies with short transition time scale as well as from the intermediate-mass LRGs by capturing stellar masses through mergers.

6. SUMMARY

We have presented the clustering analysis of LRGs selected in the HSC SSP S16A Wide layer over $\sim 124 \text{ deg}^2$ (Aihara et al. 2018). The CAMIRA algorithm (Oguri 2014) yielded 615,317 LRGs with photometric redshifts and stellar masses, enabling us to investigate the dependence of clustering and physical properties of LRGs on the redshift and the stellar mass. We derived the relationship between LRGs and their host dark haloes using the HOD formalism and compared them with those obtained in the previous HOD studies on LRGs to check the consistency as well as obtained in the photo- z -selected all galaxies. The all photo- z galaxies, which include both red and blue galaxies, are selected using the same photometric data of the HSC SSP S16A Wide

layer (Ishikawa et al. 2020) and we compare our LRG results to those from them to investigate the difference between LRGs and all photo- z galaxies.

The major findings of this study through the HOD analysis are summarized as follows:

1. Dark halo masses of central galaxies M_{\min} show the tight correlation with the number density of the LRGs irrespective of redshifts, which is consistent with previous studies. Dark halo masses with a satellite LRG M_1 also follow the power-law relation as a function of the number density as is the case with M_{\min} , although M_1 shows some redshift evolutions in the M_1 versus LRG number density relation.
2. Calculating the M_{\min} as a function of the stellar mass, M_{\min} of LRGs satisfying $M_{\star} \lesssim 10^{10.75} h^{-2} M_{\odot}$ little evolves compared to that of the all galaxy sample, indicating that the dark halo mass is the key parameter for the formation of the LRGs rather than the stellar mass. We find that $M_h \sim 10^{12.5 \pm 0.2} h^{-1} M_{\odot}$ is the critical dark halo mass for the LRG formation at least LRGs with stellar masses $M_{\star} \lesssim 10^{10.75} h^{-2} M_{\odot}$ at $0.3 < z < 1.05$. This threshold halo mass is expected to be originated from the halo quenching mechanism due to the halo environment.
3. The satellite fractions of the LRGs are much higher compared to those of the all galaxy sample at $0.1 < z < 1.05$ at all stellar-mass ranges, indicating that the LRGs tend to form pairs or small groups even at $z \sim 1$. Moreover, the high satellite fractions of LRGs are indicative of the 1-halo galactic conformity at $0.1 < z < 1.05$.
4. We find that the large-scale galaxy bias of the LRGs is monotonically increases with both the stellar mass and the redshift. At a fixed redshift, the increasing trend drastically changes at the massive end; i.e., only the most massive LRGs are highly biased objects in low- z , whereas even the intermediate-mass LRGs ($M_{\star} \sim 10^{10.5} h^{-2} M_{\odot}$) are rare at $z \sim 1$.
5. We compare the observed median halo masses of central HSC LRGs (M_{\min}) with those derived by the IllustrisTNG simulation. The median halo masses of our HSC LRGs at $0.8 \leq z \leq 1.05$ calculated by the HOD analysis show excellent agreement with those of the TNG LRGs at $z = 0.92$. This indicates that the mass measurement by our HOD analysis provides plausible results at least at $0.8 \leq z \leq 1.05$.

6. By tracing the evolution of median halo masses of red-sequence galaxies in the TNG100 simulation, the low-mass LRGs at $z \sim 1$ can evolve into intermediate-mass LRGs at $0.3 \lesssim z \lesssim 0.8$ and the high-mass LRGs at $z \sim 0.1$, whereas the massive LRGs at $z \sim 1$ are expected to grow their halo masses $\sim 10^{14} h^{-1} M_{\odot}$. Halo mass evolution indicates that the low-mass LRGs at $z \sim 1$ increase their stellar masses one magnitude order across $z = 1 - 0$. This stellar mass evolution can be achieved by galaxy mergers and satellite LRG accretions. The halo masses between the HSC LRGs at $z < 0.9$ and those evolved from the high-mass LRGs at $z \sim 1$ have a gap; however, this can be explained that most of the massive LRGs at $z < 0.9$ evolve from massive green valley galaxies with short transition time scale as well as the intermediate-mass LRGs by increasing stellar masses through mergers.

This paper presents the first clustering analysis of the HSC LRGs and demonstrates that they are an ideal sample for studying the large-scale structure. The sample used in this paper is not large enough to robustly detect signals of baryon acoustic oscillations (BAO; Eisenstein et al. 2005; Okumura et al. 2008) as well as constrain cosmological parameters. However, the latest LRG catalogue (Oguri et al. in prep.) covers enough survey volume to largely improve the detection significance of BAO. For such cosmological analysis, rather than the angular clustering analyzed in this paper, 3-dimensional clustering in redshift space will be more useful as done for a similar sample by Chiu et al. (2020). Analyzing the BAO encoded in the LRGs in the HSC survey will enable us to constrain the acoustic scale up to high redshift, $z \lesssim 1.4$.

In addition, correlation functions in redshift space also enable to test the theory of the structure formation based on the general relativity via redshift-space distortions (e.g., Davis & Peebles 1983; Guzzo et al. 2008; Okumura et al. 2016). Large and deep samples of the HSC LRG can constrain the growth rate of the Universe up to $z \sim 1.4$ with high precision by analyzing the redshift-space distortion. Moreover, combining the two-point correlation function derived in this paper with weak-lensing signals can constrain cosmological parameters since the degeneracy between cosmological parameters and the galaxy bias can be resolved (e.g., Cacciato et al. 2009; Abbott et al. 2018). We aim to probe the structure formation theory as well as the Λ CDM cosmological model using the two-point (and higher order) statistics unveiled by the HSC LRGs.

TO acknowledges support from the Ministry of Science and Technology of Taiwan under Grants No. MOST 109-2112-M-001-027- and the Career Development Award, Academia Sinica (AS-CDA-108-M02) for the period of 2019-2023. The Hyper Suprime-Cam (HSC) collaboration includes the astronomical communities of Japan and Taiwan, and Princeton University. The HSC instrumentation and software were developed by the National Astronomical Observatory of Japan (NAOJ), the Kavli Institute for the Physics and Mathematics of the Universe (Kavli IPMU), the University of Tokyo, the High Energy Accelerator Research Organization (KEK), the Academia Sinica Institute for Astronomy and Astrophysics in Taiwan (ASIAA), and Princeton University. Funding was contributed by the FIRST program from Japanese Cabinet Office, the Ministry of Education, Culture, Sports, Science and Technology (MEXT), the Japan Society for the Promotion of Science (JSPS), Japan Science and Technology Agency (JST), the Toray Science Foundation, NAOJ, Kavli IPMU, KEK, ASIAA, and Princeton University.

This paper makes use of software developed for the Large Synoptic Survey Telescope. We thank the LSST Project for making their code available as free software at <http://dm.lsst.org>

The Pan-STARRS1 Surveys (PS1) have been made possible through contributions of the Institute for Astronomy, the University of Hawaii, the Pan-STARRS Project Office, the Max-Planck Society and its participating institutes, the Max Planck Institute for Astronomy, Heidelberg and the Max Planck Institute for

Extraterrestrial Physics, Garching, The Johns Hopkins University, Durham University, the University of Edinburgh, Queen’s University Belfast, the Harvard-Smithsonian Center for Astrophysics, the Las Cumbres Observatory Global Telescope Network Incorporated, the National Central University of Taiwan, the Space Telescope Science Institute, the National Aeronautics and Space Administration under Grant No. NNX08AR22G issued through the Planetary Science Division of the NASA Science Mission Directorate, the National Science Foundation under Grant No. AST-1238877, the University of Maryland, and Eotvos Lorand University (ELTE) and the Los Alamos National Laboratory.

This paper is based on data collected at the Subaru Telescope and retrieved from the HSC data archive system, which is operated by Subaru Telescope and Astronomy Data Center at National Astronomical Observatory of Japan. Data analysis was in part carried out with the cooperation of Center for Computational Astrophysics, National Astronomical Observatory of Japan.

Numerical computations are in part carried out on the Cray XC50 (Aterui II) operated by the Center for Computational Astrophysics (CfCA), National Astronomical Observatory of Japan. Data analyses are in part carried out on the open use data analysis computer system at the Astronomy Data Center, ADC, of the National Astronomical Observatory of Japan.

Facility: Subaru Telescope (Hyper Suprime-Cam).

REFERENCES

Abbott, T. M. C., Abdalla, F. B., Alarcon, A., et al. 2018, *PhRvD*, 98, 043526. doi:10.1103/PhysRevD.98.043526

Aihara, H., Armstrong, R., Bickerton, S., et al. 2018, *PASJ*, 70, S8

Banerji, M., Ferreras, I., Abdalla, F. B., et al. 2010, *MNRAS*, 402, 2264. doi:10.1111/j.1365-2966.2009.16060.x

Bell, E. F., Wolf, C., Meisenheimer, K., et al. 2004, *ApJ*, 608, 752

Berlind, A. A., & Weinberg, D. H. 2002, *ApJ*, 575, 587

Berlind, A. A., Weinberg, D. H., Benson, A. J., et al. 2003, *ApJ*, 593, 1

Berti, A. M., Coil, A. L., Behroozi, P. S., et al. 2017, *ApJ*, 834, 87

Birnboim, Y., & Dekel, A. 2003, *MNRAS*, 345, 349

Blumenthal, G. R., Faber, S. M., Primack, J. R., et al. 1984, *Nature*, 311, 517

Brown, M. J. I., Zheng, Z., White, M., et al. 2008, *ApJ*, 682, 937

Bruzual, G. & Charlot, S. 2003, *MNRAS*, 344, 1000. doi:10.1046/j.1365-8711.2003.06897.x

Cacciato, M., van den Bosch, F. C., More, S., et al. 2009, *MNRAS*, 394, 929. doi:10.1111/j.1365-2966.2008.14362.x

Chabrier, G. 2003, *PASP*, 115, 763

Chiu, I.-N., Okumura, T., Oguri, M., Agrawal, A., Umetsu, K., & Lin, Y.-T. 2020, *MNRAS*, 498, 2030

Cooray, A. & Sheth, R. 2002, *PhR*, 372, 1

Davis, M. & Peebles, P. J. E. 1983, *ApJ*, 267, 465. doi:10.1086/160884

Dekel, A. & Birnboim, Y. 2006, *MNRAS*, 368, 2. doi:10.1111/j.1365-2966.2006.10145.x

Dekel, A., Birnboim, Y., Engel, G., et al. 2009, *Nature*, 457, 451

Eisenstein, D. J., & Hu, W. 1998, *ApJ*, 496, 605

Eisenstein, D. J., Annis, J., Gunn, J. E., et al. 2001, *AJ*, 122, 2267

Eisenstein, D. J., et al. 2005, *ApJ*, 633, 560

Fukugita, M., Ichikawa, T., Gunn, J. E., et al. 1996, *AJ*, 111, 1748

Gabor, J. M., Davé, R., Oppenheimer, B. D., et al. 2011, *MNRAS*, 417, 2676

Geha, M., Blanton, M. R., Yan, R., et al. 2012, *ApJ*, 757, 85

Groth, E. J., & Peebles, P. J. E. 1977, *ApJ*, 217, 385

Gunn, J. E., & Gott, J. R. 1972, *ApJ*, 176, 1

Guo, H., Zehavi, I., Zheng, Z., et al. 2013, *ApJ*, 767, 122

Guzzo, L., et al. 2008, *Nature*, 451, 541

Hartlap, J., Simon, P., & Schneider, P. 2007, *A&A*, 464, 399

Hartley, W. G., Conselice, C. J., Mortlock, A., et al. 2015, *MNRAS*, 451, 1613

Ishikawa, S., Kashikawa, N., Tanaka, M., et al. 2020, *ApJ*, 904, 128. doi:10.3847/1538-4357/abbd95

Kauffmann, G., Li, C., & Heckman, T. M. 2010, *MNRAS*, 409, 491

Kereš, D., Katz, N., Fardal, M., et al. 2009, *MNRAS*, 395, 160

Kravtsov, A. V., Berlind, A. A., Wechsler, R. H., et al. 2004, *ApJ*, 609, 35

Landy, S. D., & Szalay, A. S. 1993, *ApJ*, 412, 64

Ma, C.-P. & Fry, J. N. 2000, *ApJ*, 543, 503

Matsuoka, Y., Masaki, S., Kawara, K., et al. 2011, *MNRAS*, 410, 548

Miyazaki, S., Komiyama, Y., Kawanomoto, S., et al. 2018, *PASJ*, 70, S1

Moore, B., Katz, N., Lake, G., et al. 1996, *Nature*, 379, 613. doi:10.1038/379613a0

Moustakas, J., Coil, A. L., Aird, J., et al. 2013, *ApJ*, 767, 50. doi:10.1088/0004-637X/767/1/50

Navarro, J. F., Frenk, C. S., & White, S. D. M. 1997, *ApJ*, 490, 493

Norberg, P., Baugh, C. M., Gaztañaga, E., et al. 2009, *MNRAS*, 396, 19

Oguri, M. 2014, *MNRAS*, 444, 147

Oguri, M., Lin, Y.-T., Lin, S.-C., et al. 2018, *PASJ*, 70, S20

Oguri, M., Miyazaki, S., Hikage, C., et al. 2018, *PASJ*, 70, S26

Oke, J. B., & Gunn, J. E. 1983, *ApJ*, 266, 713

Okumura, T., Matsubara, T., Eisenstein, D., Kayo, I., Hikage, C., Szalay, A. S., & Schneider, D. P. 2008, *ApJ*, 676, 889

Okumura, T., Hikage, C., Totani, T., et al. 2016, *PASJ*, 68, 38. doi:10.1093/pasj/psw029

Parejko, J. K., Sunayama, T., Padmanabhan, N., et al. 2013, *MNRAS*, 429, 98

Peebles, P. J. E. 1980, *Large-Scale Structure of the Universe* by Phillip James Edwin Peebles. Princeton University Press, 1980. ISBN: 978-0-691-08240-0

Peng, Y.-. jie ., Lilly, S. J., Kovač, K., et al. 2010, *ApJ*, 721, 193

Peng, Y.-. jie ., Lilly, S. J., Renzini, A., et al. 2012, *ApJ*, 757, 4

Pillepich, A., Nelson, D., Hernquist, L., et al. 2018, *MNRAS*, 475, 648. doi:10.1093/mnras/stx3112

Planck Collaboration, Ade, P. A. R., Aghanim, N., et al. 2016, *A&A*, 594, A13

Reid, B. A., Percival, W. J., Eisenstein, D. J., et al. 2010, *MNRAS*, 404, 60

Roche, N., & Eales, S. A. 1999, *MNRAS*, 307, 703

Rozo, E., Rykoff, E. S., Abate, A., et al. 2016, *MNRAS*, 461, 1431

Salpeter, E. E. 1955, *ApJ*, 121, 161

Seljak, U. 2000, *MNRAS*, 318, 203

Sheth, R. K., & Tormen, G. 1999, *MNRAS*, 308, 119

Smith, R. E., Peacock, J. A., Jenkins, A., et al. 2003, *MNRAS*, 341, 1311

Springel, V., White, S. D. M., Tormen, G., et al. 2001, *MNRAS*, 328, 726. doi:10.1046/j.1365-8711.2001.04912.x

Spergel, D. N., Bean, R., Doré, O., et al. 2007, *ApJS*, 170, 377. doi:10.1086/513700

Springel, V., Pakmor, R., Pillepich, A., et al. 2018, *MNRAS*, 475, 676. doi:10.1093/mnras/stx3304

Takada, M., & Jain, B. 2003, *MNRAS*, 340, 580

Tanaka, M. 2015, *ApJ*, 801, 20

Tinker, J. L., Weinberg, D. H., Zheng, Z., et al. 2005, *ApJ*, 631, 41

Tinker, J. L., Robertson, B. E., Kravtsov, A. V., et al. 2010, *ApJ*, 724, 878

Totsuji, H. & Kihara, T. 1969, *PASJ*, 21, 221

van den Bosch, F. C., Yang, X., & Mo, H. J. 2003, *MNRAS*, 340, 771

van den Bosch, F. C., Aquino, D., Yang, X., et al. 2008, *MNRAS*, 387, 79

Wechsler, R. H. & Tinker, J. L. 2018, *ARA&A*, 56, 435

Weinmann, S. M., van den Bosch, F. C., Yang, X., et al. 2006, *MNRAS*, 366, 2

Wetzel, A. R., Tinker, J. L., Conroy, C., et al. 2013, *MNRAS*, 432, 336

White, S. D. M. & Rees, M. J. 1978, *MNRAS*, 183, 341

White, M., Blanton, M., Bolton, A., et al. 2011, *ApJ*, 728, 126

Woo, J., Dekel, A., Faber, S. M., et al. 2013, *MNRAS*, 428, 3306. doi:10.1093/mnras/sts274

Zehavi, I., Zheng, Z., Weinberg, D. H., et al. 2011, *ApJ*, 736, 59

Zhai, Z., Tinker, J. L., Hahn, C., et al. 2017, *ApJ*, 848, 76

Zheng, Z. 2004, *ApJ*, 610, 61

Zheng, Z., Berlind, A. A., Weinberg, D. H., et al. 2005, ApJ, 633, 791

Zheng, Z., Zehavi, I., Eisenstein, D. J., et al. 2009, ApJ, 707, 554

Zhou, R., Newman, J. A., Mao, Y.-Y., et al. 2021, MNRAS, 501, 3309. doi:10.1093/mnras/staa3764

Table 2. Best-fitting HOD Parameters of Cumulative Stellar-mass Limited LRG Samples

Redshift	Stellar-mass limit	$\log_{10} M_{\min}$	$\log_{10} M_1$	$\log_{10} M_0$	$\sigma_{\log M}$	α	f_s	b_g	$\chi^2/\text{d.o.f.}$
$0.10 \leq z < 0.30$	10.0	$11.884^{+0.049}_{-0.044}$	$13.069^{+0.111}_{-0.076}$	$10.612^{+1.326}_{-2.521}$	$0.490^{+0.247}_{-0.310}$	$1.053^{+0.125}_{-0.290}$	0.234 ± 0.037	1.154 ± 0.019	0.58
	10.25	$12.020^{+0.048}_{-0.041}$	$13.179^{+0.116}_{-0.078}$	$10.784^{+1.306}_{-3.120}$	$0.479^{+0.283}_{-0.331}$	$1.061^{+0.172}_{-0.514}$	0.230 ± 0.040	1.197 ± 0.024	0.61
	10.5	$12.186^{+0.049}_{-0.043}$	$13.344^{+0.086}_{-0.063}$	$9.072^{+2.635}_{-2.833}$	$0.487^{+0.255}_{-0.294}$	$1.138^{+0.120}_{-0.319}$	0.215 ± 0.033	1.266 ± 0.021	0.19
	10.75	$12.400^{+0.051}_{-0.042}$	$13.651^{+0.123}_{-0.113}$	$9.261^{+2.772}_{-3.025}$	$0.453^{+0.266}_{-0.277}$	$1.078^{+0.188}_{-0.386}$	0.161 ± 0.034	1.285 ± 0.020	0.13
	11.0	$12.774^{+0.051}_{-0.045}$	$14.093^{+0.312}_{-0.129}$	$9.053^{+2.836}_{-2.769}$	$0.476^{+0.262}_{-0.289}$	$1.207^{+0.343}_{-0.401}$	0.098 ± 0.034	1.428 ± 0.027	0.15
$0.30 \leq z < 0.55$	10.0	$12.224^{+0.044}_{-0.044}$	$13.064^{+0.083}_{-0.065}$	$8.602^{+2.360}_{-2.503}$	$0.545^{+0.308}_{-0.356}$	$1.119^{+0.102}_{-0.115}$	0.318 ± 0.055	1.505 ± 0.030	0.10
	10.25	$12.290^{+0.041}_{-0.040}$	$13.178^{+0.077}_{-0.063}$	$8.745^{+2.454}_{-2.584}$	$0.550^{+0.299}_{-0.352}$	$1.137^{+0.076}_{-0.163}$	0.282 ± 0.051	1.502 ± 0.030	0.11
	10.5	$12.418^{+0.042}_{-0.040}$	$13.313^{+0.098}_{-0.086}$	$10.244^{+2.038}_{-4.372}$	$0.581^{+0.302}_{-0.410}$	$1.090^{+0.145}_{-0.578}$	0.249 ± 0.054	1.492 ± 0.037	0.49
	10.75	$12.607^{+0.042}_{-0.041}$	$13.637^{+0.125}_{-0.104}$	$9.489^{+2.795}_{-3.175}$	$0.543^{+0.318}_{-0.340}$	$1.125^{+0.212}_{-0.444}$	0.177 ± 0.045	1.541 ± 0.036	0.21
	11.0	$12.967^{+0.044}_{-0.039}$	$14.020^{+0.113}_{-0.088}$	$9.423^{+2.983}_{-3.078}$	$0.540^{+0.317}_{-0.341}$	$1.310^{+0.266}_{-0.447}$	0.120 ± 0.037	1.755 ± 0.046	0.27
$0.55 \leq z < 0.80$	10.0	$12.311^{+0.039}_{-0.036}$	$13.070^{+0.067}_{-0.055}$	$8.480^{+2.293}_{-2.431}$	$0.494^{+0.240}_{-0.262}$	$1.113^{+0.065}_{-0.075}$	0.330 ± 0.043	1.723 ± 0.026	0.08
	10.25	$12.366^{+0.041}_{-0.036}$	$13.227^{+0.058}_{-0.048}$	$8.592^{+2.466}_{-2.460}$	$0.497^{+0.241}_{-0.269}$	$1.182^{+0.081}_{-0.090}$	0.269 ± 0.039	1.722 ± 0.028	0.08
	10.5	$12.486^{+0.042}_{-0.037}$	$13.392^{+0.078}_{-0.059}$	$8.834^{+2.559}_{-2.645}$	$0.497^{+0.236}_{-0.268}$	$1.186^{+0.092}_{-0.224}$	0.228 ± 0.037	1.749 ± 0.029	0.10
	10.75	$12.671^{+0.039}_{-0.034}$	$13.673^{+0.077}_{-0.074}$	$9.113^{+2.691}_{-2.808}$	$0.486^{+0.253}_{-0.258}$	$1.180^{+0.119}_{-0.311}$	0.166 ± 0.033	1.807 ± 0.033	0.21
	11.0	$13.016^{+0.039}_{-0.037}$	$13.991^{+0.094}_{-0.094}$	$9.517^{+2.953}_{-3.155}$	$0.520^{+0.215}_{-0.280}$	$1.176^{+0.198}_{-0.381}$	0.133 ± 0.035	2.030 ± 0.042	0.17
$0.80 \leq z \leq 1.05$	10.0	$12.367^{+0.038}_{-0.035}$	$13.202^{+0.053}_{-0.043}$	$8.410^{+2.306}_{-2.250}$	$0.636^{+0.245}_{-0.499}$	$1.265^{+0.076}_{-0.074}$	0.205 ± 0.056	1.815 ± 0.051	0.54
	10.25	$12.450^{+0.037}_{-0.034}$	$13.297^{+0.057}_{-0.048}$	$8.368^{+2.304}_{-2.316}$	$0.575^{+0.298}_{-0.402}$	$1.257^{+0.078}_{-0.078}$	0.206 ± 0.050	1.900 ± 0.050	0.46
	10.5	$12.614^{+0.039}_{-0.034}$	$13.486^{+0.075}_{-0.058}$	$8.910^{+2.557}_{-2.652}$	$0.589^{+0.279}_{-0.347}$	$1.265^{+0.088}_{-0.502}$	0.167 ± 0.045	1.959 ± 0.052	0.22
	10.75	$12.818^{+0.041}_{-0.034}$	$13.788^{+0.080}_{-0.066}$	$9.076^{+2.743}_{-2.711}$	$0.499^{+0.322}_{-0.299}$	$1.369^{+0.212}_{-0.292}$	0.119 ± 0.034	2.192 ± 0.058	0.08
	11.0	$13.357^{+0.038}_{-0.035}$	$14.479^{+0.317}_{-0.197}$	$9.428^{+3.096}_{-3.021}$	$0.635^{+0.245}_{-0.399}$	$1.346^{+0.391}_{-0.407}$	0.034 ± 0.027	2.466 ± 0.096	0.12

NOTE—The stellar-mass limit is in units of $h^{-2} M_{\odot}$ in a logarithmic scale, whereas all halo-mass parameters are in units of $h^{-1} M_{\odot}$.